Supplement of

Predicting photooxidant concentrations in aerosol liquid water based on laboratory extracts of ambient particles

Lan Ma[1a], Reed Worland[1b], Wenqing Jiang[2], Christopher Niedek[2], Chrystal Guzman[1c], Keith J. Bein[3], Qi Zhang[2], Cort Anastasio[1]

[1]Department of Land, Air and Water Resources, University of California, Davis, One Shields Avenue, Davis, CA 95616-8627, USA

[2]Department of Environmental Toxicology, University of California, Davis, One Shields Avenue, Davis, CA 95616-8627, USA

[3]Center for Health and the Environment, University of California, Davis, One Shields Avenue, Davis, CA 95616-8627, USA

[a]Now at: SGS-CSTC Standards Technical Services Co.,Ltd. Hangzhou Branch, Hangzhou, Zhejiang Province, 310052, China

[b]Now at Department of Chemistry, University of Washington, 1410 Northeast Campus Parkway, Seattle, WA 98195, USA

[c]Now at Department of Pharmacology, University of Washington, 1410 Northeast Campus Parkway, Seattle, WA 98195, USA

Correspondence to: Cort Anastasio (canastasio@ucdavis.edu)

Table of contents

Table S1. Particle sample collection and PME information

Sample ID[a]	Collection dates[b]	Sampling duration for each filter (h)	Average $PM_{2.5}$ concentration[d] ($\mu g/m^3$-air)	Particle mass/water ratio[e] (10^{-4} μg PM/μg H_2O)	α_{300}[f] (cm^{-1})	R_{abs} (300-450 nm) (10^{-6} mol-photons $L^{-1}s^{-1}$)[g]	AAE[h]	MAC_{DOC} (300nm) (m^2 (g C)$^{-1}$)[i]	MAC_{DOC} (365nm) (m^2 (g C)$^{-1}$)[i]	DOC (mg C L^{-1})	Light screening factor[j]	
											PME	PME+ DMB
WIN-10	2/5/20 – 2/28/20	168[c] (one week)	9.2	0.51 (±0.09)	0.086	1.5	7.58	2.0	0.57	10.1	0.98	0.75
WIN-2				2.6 (±0.4)	0.446	7.8	7.28	2.2	0.65	47.2	0.88	N.A.
WIN-0.7				5.5 (±0.9)	1.089	19	7.23	2.5	0.74	102.1	0.74	0.64
WIN-0.4				10 (±1.5)	1.820	33	7.02	2.0	0.63	206.3	0.61	N.A.
WIN-0.3				16 (±2.4)	3.029	56	7.00	2.1	0.65	335.6	0.48	0.40[k]
WIN-0.3D				2.4 (±0.4)	0.452	8.1	7.16	2.1	0.64	50.2	0.88	0.73
SUM-10	8/21/20 – 8/24/20	28.8[c]	54.5	0.42 (±0.07)	0.220	3.9	7.42	3.1	0.96	16.4	0.94	0.75
SUM-2				2.1 (±0.4)	1.062	20	7.17	3.4	1.07	72.7	0.74	N.A.
SUM-0.7				5.5 (±1.3)	2.780	51	7.17	3.1	0.97	208.9	0.50	0.46
SUM-0.4				11 (±2.3)	5.147	97	7.05	3.1	0.99	383.4	0.32	N.A.
SUM-0.3				14 (±2.4)	6.679	128	6.93	3.1	1.01	495.4	0.26	0.23[k]
PME-NR[l]	10/6/20 – 10/8/20	48	30.9	6.4 (±0.2)	1.504	22	7.57	1.7	0.40	209.9	0.70	0.61
PME-R[m]				6.4 (±0.3)	1.579	23	7.74	1.8	0.44	204.3	0.68	0.60
Field blanks[n]												
FB1	8/4/20	3 min	6.9	0.16 (±0.06)	0.0022	0.017				2.1	1	
FB2	1/2/20	3 min	15.6	0.13 (±0.06)	0.0015	0.0013				2.0	1	
FB3	10/5/20	3 min	39.6	0.47 (±0.38)	0.0065	0.086				3.0	1	

[a] Samples were named as "PME-water volume" (e.g., WIN-0.7) to denote the sample and extraction volume. WIN-0.3D is the WIN-0.3 sample diluted to an equivalent extract volume of 2 mL/square (i.e., to the equivalent dilution of WIN-2).

[b] For the WIN and SUM samples, we collected three separate, consecutive filters during each collection period and then composited them during extraction. Each winter filter was collected for a week, while each summer filter was collected for approximately 29 hrs. The 10/6/20-10/8/20 sample was just one filter collected for 48 h.

[c] The average sampling duration for each filter within a given composite.

[d] Average $PM_{2.5}$ concentration for each sampling period measured at the UC Davis sampling site by the California Air Resources as reported on the *i*ADAM online database (California Air Resources Board, 2019 −2020; https://www.arb.ca.gov/adam).

[e] Particle mass/water mass ratio (±1 σ) is calculated as the extracted particle mass per filter square (determined as the difference of filter weights before and after extraction) divided by the volume of water used for extraction.

[f] Base-10 absorbance coefficient of the extract (in cm^{-1}) at 300 nm. This is determined as the sample absorbance divided by the cell pathlength.

[g] Rate of sunlight absorption by PME in the 300-450 nm wavelength range, calculated by equation 2 in Kaur et al. (2019), using the actinic flux at midday on the winter solstice in Davis (photons cm^{-2} s^{-1} nm^{-1}) obtained from the Tropospheric Ultraviolet and Visible (TUV) Radiation Model version 4.1. If we apply the actinic flux at midday on the summer solstice, the rate of light absorption is larger by a factor 1.9.

[h] AAE, the Angstrom Absorption Exponent, is calculated as the negative slope of a linear regression between ln(absorbance) vs. ln(wavelength) in the 300 – 450 nm wavelength range.

[i] Mass absorption coefficients at 300 or 365 nm, normalized to dissolved organic carbon, calculated as $MAC_{DOC,300nm} = \frac{\alpha_{300nm,} \times \ln(10) \times 10^6}{[DOC]}$ (Kaur et al., 2019). The contributions of nitrate and nitrite to the total absorbance of PME samples are negligible (< 2 %) for both wavelengths.

[j] Light-absorption-weighted internal screening factor, calculated with equation 2 in Smith et al. (2016) using a wavelength range of 280-364 nm. A value of 1 indicates no light screening, while a low value represents a strong screening effect. "PME" column shows light screening factors in PME samples, while "PME+DMB" column shows values in the PME with added 80 µM DMB (used for inhibition factor measurements; see Section S1). The cell pathlength was 0.5 cm. To save sample volume, *IF* values were not measured for the -2 and -0.4 extracts, so screening factors are not available for these dilutions.

[k] For these very concentrated PME samples, 160 µM DMB was used for inhibition factor measurements. Values shown here are light screening factors of PME with 160 µM DMB.

[l] This sample was extracted with 0.7 mL water/square and is not rotovapped.

[m] This sample was extracted using the same filter as PME-NR, with 2 mL water/square, and then rotovapped to an equivalent extract volume of 0.7 mL/square.

[n] Field blank samples were extracted with 1.0 mL water/square.

Table S2. Ion concentrations in PMEs

Sample ID	$[NO^{3-}]$ (µM)	$[NO_2^-]$ (µM)	$[SO_4^{2-}]$ (µM)[a]	$[Cl^-]$ (µM)	$[HCOO^-]$ (µM)	$[NH_4^+]$ (µM)	$[Na^+]$ (µM)	$[K^+]$ (µM)	$[Ca^{2+}]$ (µM)
WIN-10	179.1	< DL[d]	25.0	5.21	2.65	160.8	196.3	34.0	68.8
WIN-2	793.1	3.49	346.9	29.3	30.3	590.4	612.1	98.4	240.3
WIN-0.7	1535	6.49	538.8	20.5	45.9	1826.7	1238.3	261.4	449.9
WIN-0.4	3215	13.6	1435	89.7	116.4	2558.6	2543.9	457.3	149.4
WIN-0.3	5221	21.3	2347	129.2	193.6	3898.2	3601.5	658.4	1214
WIN-0.3D[b]									
SUM-10	27.4	< DL	21.4	5.21	3.53	100.8	134.2	31.5	50.4
SUM-2	137.6	1.95	90.3	23.4	46.0	208.1	276.0	101.1	98.1
SUM-0.7	325.9	2.49	194.1	64.2	92.8	676.4	607.5	315.8	70.5
SUM-0.4	777.7	< DL	478.0	144.7	145.5	1125	1360	561.3	578.6
SUM-0.3	1018	7.85	618.2	184.2	187.9	1330	1717	676.4	696.7
PME-NR	487.0	8.00	352.7	5.21	3.53	1565	1458	356.5	606.6
PME-R	479.7	8.00	349.1	23.4	46.0	1496	1201	517.0	526.7
Field blanks									
FB1[c]	3.12	<DL		2458	3.03	0.12	96.0	-0.02	7.01
FB2	4.58	<DL		1.07	2.94	1.42	93.8	5.92	7.02
FB3	1.99	<DL	12.41	0.65	5.54	1.11	124.6	8.88	7.08

[a] The amount of sulfuric acid added to adjust sample pH has been subtracted. The added sulfuric acid has an average (± σ) of 40 (± 47) µM.

[b] Ion concentrations were not measured in this sample.

[c] This field blank sample was contaminated by the pH electrode filling solution, resulting in extremely high concentrations of Cl^- and possible other, uncharacterized, contaminants.

[d] Below detection limit.

Table S3. Hydroxyl radical measurements

Sample ID	P_{OH} (10^{-9} $M^{-1}s^{-1}$)[a]	k'_{OH} (10^{6} s^{-1})[b]	[•OH] (10^{-15} M)[c]	$10^{4} \times \Phi_{OH}$[d]	k_{DOC+OH} (10^{8} L (mol-C)$^{-1}$ s^{-1})[e]	$\%P_{OH,NO3-}$[f]
WIN-10	0.24 (± 0.01)	0.20 (± 0.03)	1.2 (± 0.2)	1.7 (± 0.1)	4.5 (± 0.4)	10.4
WIN-2	4.6 (± 0.4)	8.82 (± 0.09)	5.6 (± 0.4)	5.8 (± 0.5)	3.1 (± 0.3)	2.4
WIN-0.7	16.4 (± 1.5)	2.2 (± 0.2)	7.4 (± 0.2)	8.6 (± 0.8)	1.6 (± 0.8)	1.3
WIN-0.4	21.3 (± 5.3)	2.6 (± 0.7)	6.8 (± 0.5)	6.3 (± 1.6)	2.5 (± 0.5)	2.1
WIN-0.3	47.5 (± 41.2)	9.9 (± 8.6)	4.8 (± 0.3)	8.5 (± 7.4)	2.6 (± 3.1)	1.5
WIN-0.3D			4.1 (± 0.4)			
SUM-10	0.26 (± 0.01)	0.61 (± 0.06)	0.43 (± 0.01)	0.67 (± 0.03)	2.4 (± 0.4)	1.5
SUM-2	1.8 (± 0.1)	1.9 (± 0.2)	1.0 (± 0.01)	0.94 (± 0.07)	2.1 (± 0.2)	1.0
SUM-0.7	12.3 (± 5.7)	2.8 (± 1.4)	4.4 (± 0.6)	2.4 (± 1.1)	2.6 (± 0.3)	0.4
SUM-0.4	57.3 (± 10.7)	8.0 (± 1.5)	7.2 (± 0.1)	5.9 (± 1.1)	1.5 (± 0.4)	0.2
SUM-0.3	81.5(± 98.4)	10.6 (± 12.8)	7.7 (± 0.7)	6.4 (± 7.7)	3.5 (± 3.1)	0.2
PME-NR			4.2 (± 0.3)			
PME-R			4.6 (± 0.8)			
Field blanks						
FB1[g]			0.57 (± 0.03)			
FB2[h]	0.0011 (± 0.0001)	0.20 (± 0.02)	0.06 (± 0.01)			5.7
FB3[h]	0.0008 (± 0.0001)	0.05 (± 0.02)	0.15 (± 0.01)			3.6

[a] Davis winter solstice-normalized rate of •OH photoproduction.

[b] Apparent pseudo-first-order rate constant for destruction of •OH due to natural sinks.

[c] Winter solstice-normalized steady-state concentration of •OH.

[d] Apparent quantum yield of •OH during simulated sunlight illumination, calculated as $\Phi_{OH} = P_{OH}/R_{abs}$

[e] Second-order rate constant of dissolved organic carbon scavenging •OH, calculated as $k_{DOC+OH} = k'_{OH}/DOC$. The average (± 1σ) values for this rate constant in WIN and SUM dilutions were 2.4 × (±0.7) ×10^{8} L (mol-C)$^{-1}$ s^{-1} and 2.9 × (±1.1) ×10^{8} L (mol-C)$^{-1}$ s^{-1}, respectively.

[f] Fraction of nitrate contribution to the •OH photoproduction rate, calculated as ($j_{NO3-\rightarrow OH}$ × [NO_3^-]/P_{OH}) using the aqueous nitrate photolysis rate constant, $j_{NO3-\rightarrow OH} = 1.4 \times 10^{-7}$ s^{-1} (Anastasio and McGregor, 2001) and the molar concentration of NO_3^-. We also calculated the fraction of •OH production rate due to nitrite: it is negligible, with an average value of 1 %.

[g] This field blank sample was contaminated by the pH electrode.

[h] The •OH production rate in field blanks was determined by adding 1.2 mM benzoic acid to 1.0 mL FB sample and monitoring the formation of *p*-hydroxybenzoic acid, assuming that all •OH produced reacts with benzoic acid.

Table S4. Rate constants of SYR and PTA reacting with triplet excited states, singlet oxygen, and hydroxyl radical at pH 4.2

Oxidants	k_{SYR+Ox} (M^{-1} s^{-1})	Reference	k_{PTA+Ox} (M^{-1} s^{-1})	Reference
$^{\bullet}OH$	20 (±4) × 10^9	(Smith et al., 2015)	10.3 (±0.6) × 10^9	(Ma et al., 2023)
$^1O_2$*	3.6 (±0.7) × 10^7	(Tratnyek and Hoigne, 1991)	8.8 (±0.6) × 10^6	
^{3}DMB*	3.9 (±0.7) × 10^9	(Smith et al., 2015)	2.5 (±0.6) ×10^9	
Direct photodegradation	j_{SYR} (s^{-1})		j_{PTA} (s^{-1})	
	< 4.3 × 10^{-6}	(Kaur and Anastasio, 2018)	6.2 (±0.2) × 10^{-4}	(Ma et al., 2023)

Table S5. Syringol loss kinetics and resulting triplet excited state concentrations

Sample ID	k'_{SYR}[a] (10^{-2} min^{-1})	$f_{SYR,OH}$[b]	$f_{SYR,1O2*}$[c]	$f_{SYR,3C*}$[d]	$[^3C*]_{SYR,uncorr}$[e] (10^{-14} M)	$[^3C*]_{SYR}$[f] (10^{-14} M)	$k'_{3C*,SYR}$[g] (10^6 s^{-1})	$P_{3C*,SYR}$[h] (10^{-7} M s^{-1})	$10^2 \times \Phi_{3C*,SYR}$[i]
WIN-10	0.63 (±0.03)	0.23 (±0.06)	0.07 (±0.02)	0.70 (±0.07)	1.9 (±0.4)	4.8 (±1.0)	0.85	0.40 (±0.09)	2.8 (±0.6)
WIN-2	1.9 (±0.1)	0.35 (±0.08)	0.13 (±0.03)	0.52 (±0.09)	4.2 (±1.0)	15 (±4)	1.1	1.6 (±0.5)	2.1 (±0.6)
WIN-0.7	3.7 (±0.2)	0.24 (±0.05)	0.14 (±0.04)	0.62 (±0.09)	9.8 (±2.3)	50 (±16)	1.4	7.2 (±2.4)	3.7 (±1.2)
WIN-0.4	4.6 (±0.2)	0.18 (±0.04)	0.20 (±0.06)	0.62 (±0.08)	12 (±3)	71 (±22)	2.1	15 (±5)	4.4 (±1.3)
WIN-0.3	3.9 (±0.2)	0.15 (±0.03)	0.45 (±0.10)	0.40 (±0.11)	6.7 (±2.3)	50 (±20)	2.9	15 (±6)	2.6 (±1.0)
WIN-0.3D	1.7 (±0.1)	0.28 (±0.06)	0.12 (±0.03)	0.60 (±0.09)	4.5 (±1.0)	16 (±5)	1.1	1.8 (±0.5)	2.2 (±0.6)
SUM-10	2.2 (±0.1)	0.02 (±0.01)	0.03 (±0.01)	0.95 (±0.03)	8.9 (±1.6)	16 (±3)	0.94	1.5 (±0.3)	3.8 (±0.7)
SUM-2	4.5 (±0.1)	0.03 (±0.01)	0.10 (±0.02)	0.87 (±0.03)	17 (±3)	32 (±7)	1.5	4.8 (±1.1)	2.4 (±0.5)
SUM-0.7	8.7 (±0.3)	0.06 (±0.01)	0.13 (±0.03)	0.81 (±0.04)	31 (±6)	68 (±18)	2.8	19 (±5)	3.7 (±1.0)
SUM-0.4	7.9 (±0.1)	0.11 (±0.02)	0.21 (±0.04)	0.68 (±0.05)	23 (±5)	68 (±18)	4.5	31 (±8)	3.2 (±0.9)
SUM-0.3	7.3 (±0.1)	0.13 (±0.03)	0.25 (±0.09)	0.62 (±0.10)	20 (±6)	65 (±20)	5.6	36 (±11)	2.8 (±0.9)
PME-NR	10.7 (±0.3)	0.05 (±0.01)	0.06 (±0.01)	0.89 (±0.03)	41 (±8)	54 (±28)	2.0	11 (±6)	5.0 (±2.6)
PME-R	11.2 (±0.4)	0.05 (±0.01)	0.05 (±0.01)	0.90 (±0.04)	43 (±8)	69 (±15)	2.0	14 (±3)	5.9 (±1.3)
Field blanks									
FB1[j]	0.031 (±0.002)	2.20 (±1.34)	0.11 (±0.02)	-1.31 (±1.34)	-0.018 (±0.018)	-0.32 (±0.33)			
FB2	0.008 (±0.001)	0.09 (±0.02)	0.05 (±0.01)	0.86 (±0.03)	0.30 (±0.05)	0.32 (±0.08)			
FB3	0.12 (±0.01)	0.15 (±0.04)	0.05 (±0.01)	0.80 (±0.06)	0.42 (±0.08)	0.42 (±0.08)			

[a] Davis winter-solstice-normalized pseudo-first-order rate constant for loss of syringol (SYR).

[b] Fraction of SYR loss due to hydroxyl radical, calculated as $f_{SYR,OH} = (k_{SYR+OH} \times [^{\bullet}OH])/k'_{SYR}$. Hydroxyl radical concentrations are in Table S5.

[c] Fraction of SYR loss due to singlet oxygen, calculated as $f_{SYR,1O2*} = (k_{SYR+1O2*} \times [^1O_2*])/k'_{SYR}$. Singlet oxygen concentrations are in Table S8.

[d] Fraction of SYR loss due to triplets, calculated as $f_{SYR,3C*} = (1 - f_{SYR,OH} - f_{SYR,1O2*})$.

[e] Uncorrected triplet steady-state concentration calculated from syringol loss as $k'_{SYR,3C*}/k_{SYR+3DMB*}$.

[f] Triplet concentration after correction for inhibition of SYR loss, calculated as $[^3C*]_{SYR,uncorr}/IF_{SYR,corr}$.

[g] Apparent pseudo-first-order rate constant for quenching of $^3C*$ due to natural organic sinks and dissolved oxygen, as determined by SYR. This was calculated as $k'_{3C*,SYR} = k_{rxn+Q,3C*}[DOC] + k_{3C*+O2}[O_2]$, where $k_{rxn+Q,3C*}$ is estimated from the fitting between $[^3C*]_{SYR}$ and DOC using equation (11) in the main text (see values in Table S9), and $k_{3C*+O2} = 2.8 (\pm 0.4) \times 10^9$ M^{-1} s^{-1} from Kaur et al. (2019).

[h] Production rate of triplets determined by SYR, calculated as $P_{3C*,SYR} = [^3C*]_{SYR} \times k'_{3C*,SYR}$.

[i] Apparent quantum yield of $^3C*$ determined by SYR during simulated sunlight illumination, calculated as $\Phi_{3C*,SYR} = P_{3C*,SYR}/R_{abs}$.

[j] This field blank sample was contaminated by filling solution from a pH electrode.

Table S6. (Phenylthio)acetic acid (PTA) loss kinetics and resulting triplet excited state concentrations

Sample ID	k'_{PTA}[a] (10^{-2} min^{-1})	$f_{PTA,OH}$[b]	$f_{PTA,1O2*}$[c]	$f_{PTA,3C*}$[d]	$[^3C*]_{PTA,uncorr}$[e] (10^{-14} M)	$[^3C*]_{PTA}$[f] (10^{-14} M)	$k'_{3C*,PTA}$[g] (10^6 s^{-1})	$P_{3C*,PTA}$[h] (10^{-7} M s^{-1})	$10^2 \times \Phi_{3C*,PTA}$[i]	$[^3C*]_{PTA}/[^3C*]_{SYR}$[j]
WIN-10	0.45 (±0.02)	0.17 (±0.03)	0.02 (±0.01)	0.81 (±0.06)	2.4 (±0.06)	2.4 (±0.06)	0.83	0.20 (±0.05)	1.4 (±0.3)	0.51 (±0.17)
WIN-2	2.3 (±0.1)	0.15 (±0.01)	0.03 (±0.01)	0.82 (±0.02)	13 (±3)	13 (±3)	1.0	1.3 (±0.3)	1.6 (±0.4)	0.84 (±0.31)
WIN-0.7	3.8 (±0.1)	0.12 (±0.01)	0.03 (±0.01)	0.85 (±0.04)	22 (±5)	22 (±5)	1.3	2.8 (±0.7)	1.4 (±0.4)	0.43 (±0.18)
WIN-0.4	6.1 (±0.3)	0.07 (±0.01)	0.04 (±0.01)	0.89 (±0.05)	36 (±9)	36 (±9)	1.8	6.4 (±1.6)	1.9 (±0.5)	0.51 (±0.20)
WIN-0.3	6.6 (±0.3)	0.05 (±0.01)	0.06 (±0.01)	0.89 (±0.03)	39 (±10)	39 (±10)	2.4	9.3 (±3.0)	1.8 (±0.5)	0.78 (±0.39)
WIN-0.3D	2.5 (±0.1)	0.10 (±0.01)	0.02 (±0.01)	0.88 (±0.02)	15 (±4)	15 (±4)	1.0	1.6 (±0.5)	1.9 (±0.6)	0.95 (±0.39)
SUM-10	0.57 (±0.02)	0.05 (±0.01)	0.03 (±0.02)	0.92 (±0.04)	0.35 (±0.09)	0.37 (±0.10)	0.87	0.33 (±0.08)	0.85 (±0.21)	0.23 (±0.07)
SUM-2	2.1 (±0.1)	0.03 (±0.01)	0.06 (±0.01)	0.91 (±0.03)	13 (±3)	13 (±4)	1.2	1.6 (±0.4)	0.80 (±0.22)	0.41 (±0.15)
SUM-0.7	3.5 (±0.1)	0.08 (±0.01)	0.08 (±0.01)	0.84 (±0.02)	20 (±5)	21 (±6)	1.9	4.0 (±1.1)	0.78 (±0.22)	0.30 (±0.12)
SUM-0.4	4.9 (±0.1)	0.10 (±0.01)	0.08 (±0.01)	0.82 (±0.03)	27 (±7)	27 (±8)	2.9	7.9 (±2.2)	0.81 (±0.23)	0.40 (±0.16)
SUM-0.3	5.2 (±0.2)	0.09 (±0.01)	0.09 (±0.03)	0.82 (±0.03)	29 (±7)	29 (±8)	3.5	10 (±3)	0.78 (±0.22)	0.44 (±0.19)
PME-NR	4.4 (±0.1)	0.06 (±0.01)	0.03 (±0.01)	0.91 (±0.03)	27 (±7)	28 (±16)	2.1	5.8 (±3.2)	2.6 (±1.5)	0.52 (±0.40)
PME-R	4.8 (±0.1)	0.06 (±0.01)	0.03 (±0.01)	0.91 (±0.02)	29 (±7)	41 (±10)	2.0	8.4 (±2.1)	3.6 (±0.1)	0.60 (±0.20)
Field blanks										
FB1[k]	2.75 (±0.04)	0.01 (±0.01)	0.00 (±0.01)	0.99 (±0.14)	18.1 (±5.0)	20.1 (±7.0)				
FB2	0.016 (±0.005)	0.22 (±0.03)	0.07 (±0.01)	0.71 (±0.32)	0.078 (±0.040)	0.084 (±0.043)				
FB3	0.030 (±0.012)	0.31 (±0.04)	0.05 (±0.01)	0.64 (±0.38)	0.13 (±0.08)	0.13 (±0.08)				

[a] Davis winter-solstice-normalized value of the measured pseudo-first-order rate constant for loss of PTA after correction for PTA direct photodegradation. PTA direct photodegradation accounted for (0.9-12) % of PTA total decay in PME samples, with an average of 3%. It accounted for (2-79) % of PTA total decay in field blanks.

[b] Contribution of hydroxyl radical to the loss of PTA, calculated as $f_{PTA,OH} = (k_{PTA+OH} \times [^{\bullet}OH])/k'_{PTA}$. Hydroxyl radical concentrations are in Table S5.

[c] Contribution of singlet oxygen to the loss of PTA, calculated as $f_{PTA,1O2*} = (k_{PTA+1O2*} \times [^1O_2*])/k'_{PTA}$. Singlet oxygen concentration is in the Table S8.

[d] Fraction of PTA loss due to triplets, calculated as $f_{PTA,3C*} = (1 - f_{PTA,OH} - f_{PTA,1O2*})$.

[e] Uncorrected triplet steady-state concentration calculated from PTA loss as $k'_{PTA,3C*}/k_{PTA+3DMB*}$.

[f] Triplet concentration after correction for inhibition of PTA loss, calculated as $[^3C*]_{PTA,uncorr}/IF_{PTA,corr}$.

[g] Apparent pseudo-first-order rate constant for quenching of $^3C*$ determined by PTA due to natural organic sinks and dissolved oxygen. This was calculated as $k'_{3C*,PTA} = k_{rxn+Q,3C*}[DOC] + k_{3C*+O2}[O_2]$, where $k_{rxn+Q,3C*}$ is estimated from the fitting between $[^3C*]_{PTA}$ and DOC using equation (10) in the main text (values are in Table S9), and $k_{3C*+O2} = 2.8 (\pm 0.4) \times 10^9$ M^{-1} s^{-1} from Kaur et al. (2019).

[h] Production rate of triplet determined by PTA, calculated as $P_{3C*,PTA} = [^3C*]_{PTA} \times k'_{3C*,PTA}$.

[i] Apparent quantum yield of $^3C^*$ determined by PTA during simulated sunlight illumination, calculated as $\Phi_{3C^*,PTA} = P_{3C^*,PTA}/R_{abs}$.

[j] Ratio of triplet concentration determined by PTA to that determined by SYR.

[k] This field blank sample was contaminated by a pH electrode, leading to fast decay of PTA.

Section S1. Inhibition factor determination and ^{3}C* concentration correction

Dissolved organic matter in PME may inhibit the decay of SYR or PTA by triplets, leading to an underestimation of triplet concentration. Based on our previous research, SYR is more strongly inhibited than PTA (Ma et al., 2023). To investigate and quantify the inhibition effect of PME on these two triplet probes, we measured inhibition factors (*IF*s) of FFA, SYR, and PTA for the -10, -0.7 and -0.3 extracts of the WIN and SUM composites, and used the *IF* values to correct measured ^{3}C* concentrations in PME. Details of inhibition factors are described in Canonica et al. (2008), Wenk et al. (2011), and Ma et al. (2023). To measure *IF*, we monitored the loss of 10 μM probe in three illuminated solutions: (1) in the pH 4.2 PME; (2) in pH 4.2 Milli-Q water containing 80 μM of triplet precursor 3,4-dimethoxybenzaldehyde (DMB); and (3) in the PME with added DMB (80 μM DMB for the -10 extract and 160 μM DMB for the -0.7 and -0.3 extracts). For each illumination, we determined the first-order rate constant of probe decay. The inhibition factor for the probe in that extract was calculated using

$$IF_P = \frac{k'_{DMB,PME} - k'_{PME}}{k'_{DMB}} \quad (S1)$$

where $k'_{DMB,PME}$ is the first-order decay rate constant of probe in solution containing both DMB and PME, while k'_{PME} and k'_{DMB} are the probe loss rate constants in PME alone and in Milli-Q water with DMB, respectively. All *k'* values were corrected for internal light screening with screening factors (S_λ); the PME and PME+DMB values are listed in Table S1, while the light screening factors for 80 and 160 μM DMB are 0.75 and 0.59, respectively. An *IF* value of 1 indicates there is no DOM inhibition on probe decay, while *IF* = 0 indicates complete inhibition of probe decay. Since IF_P can also be affected by DOM suppressing the ^{3}DMB* concentration, we use IF_{FFA} to quantify this triplet suppression (Ma et al., 2023). To exclude the effect of triplet suppression on IF_{SYR} and IF_{PTA} (i.e., to quantify only inhibition due to probe regeneration), we use corrected inhibition factors, $IF_{SYR,corr}$ and $IF_{PTA,corr}$:

$$IF_{P,corr} = \frac{IF_P}{IF_{FFA}} \quad (S2)$$

Theoretically, *IF* should not exceed 1, but we sometimes see this result. When IF_{FFA} or IF_P is greater than 1, it suggests there is interaction between DOM in PME with DMB to form reactive species, and thus indicates no inhibition or suppression. Therefore, when IF_{FFA} and/or IF_P is greater than 1, we assume that $IF_{P,corr} = IF_P$, but we do not correct the ^{3}C* concentration if $IF_{P,corr} \geq 1$; i.e., in this latter case $[^3C^*]_P = [^3C^*]_{P,uncorr}$. More details are provided in Ma et al. (2023). IF_{PTA} and IF_{SYR} values are expected to be lower than IF_{FFA} because IF_{PTA} and IF_{SYR} are affected by both triplet suppression by DOC and probe inhibition by DOC, while IF_{FFA} is only impacted by triplet suppression. However, in some samples IF_{PTA} was

greater than IF_{FFA}; we suspect this might be due to the sometimes large errors in IF_{FFA} measurement, i.e., when the difference between $k'_{DMB,PME}$ and k'_{PME} is small. In this case, we assume $IF_{FFA} = IF_{PTA}$ (since PTA is very resistant to suppression) and use this value to calculate $IF_{P,corr}$. The determined *IF* and $IF_{P,corr}$ values are shown in Table S4. Due to limited PME volumes, we did not measure *IF* values for the -2 and -0.4 extracts. Instead, their $IF_{SYR,corr}$ and $IF_{PTA,corr}$ values were estimated from the linear regression of $1/IF_{P,corr}$ from the -10, -0.7, and -0.3 extracts versus DOC (Ma et al., 2023; Wenk et al., 2011).

The uncorrected ^{3}C* concentration is calculated with:

$$[^3C^*]_{P,uncorr} = \frac{k'_{P,3C*}}{k_{P+3DMB*}} \quad (S3)$$

where $k'_{P,3C*}$ is the measured first-order rate constant of probe loss due to triplets and $k_{P+3DMB*}$ is the second-order rate constant of probe reacting with ^{3}DMB*. This assumes that the DMB triplet is a reasonable proxy for triplets in atmospheric particles and drops in Davis, as we have shown previously (Kaur and Anastasio, 2018; Kaur et al., 2019). To correct for the probe inhibition effect, [^{3}C*] is calculated using

$$[^3C^*]_P = \frac{[^3C^*]_{P,uncorr}}{IF_{P,corr}} \quad (S4)$$

The ^{3}C* concentrations shown in the main text are the values after *IF* correction.

Table S7. Inhibition factors for FFA, SYR, and PTA

Sample ID	IF_{FFA}	IF_{SYR}	IF_{PTA}	$IF_{SYR,corr}$	$IF_{PTA,corr}$
WIN-10	0.91 (±0.06)	0.40 (±0.02)	1.00 (±0.04)	0.41 (±0.03)	1.00 (±0.06)
WIN-2[a]				0.28 (±0.04)	1.00 (±0.09)
WIN-0.7	0.62 (±0.10)	0.18 (±0.03)	0.90 (±0.07)	0.20 (±0.04)	1.00 (±0.11)
WIN-0.4[a]				0.17 (±0.04)	1.00 (±0.16)
WIN-0.3	0.28 (±0.08)	0.09 (±0.01)	0.67 (±0.10)	0.13 (±0.03)	1.00 (±0.21)
WIN-0.3D[b]	0.89 (±0.13)	0.25 (±0.02)	0.85 (±0.06)	0.28 (±0.05)	0.97 (±0.17)
SUM-10	1.08 (±0.09)	0.56 (±0.02)	0.95 (±0.08)	0.56 (±0.02)	0.94 (±0.07)
SUM-2[a]				0.53 (±0.07)	0.95 (±0.12)
SUM-0.7	0.48 (±0.06)	0.22 (±0.03)	0.46 (±0.04)	0.45 (±0.09)	0.96 (±0.14)
SUM-0.4[a]				0.35 (±0.06)	0.98 (±0.14)
SUM-0.3	0.19 (±0.12)	0.10 (±0.02)	0.32 (±0.03)	0.30 (±0.06)	1.00 (±0.14)
PME-NR[c]	0.68 (±0.32)	0.52 (±0.05)	0.65 (±0.04)	0.77 (±0.37)	0.95 (±0.48)
PME-R[c]	1.29 (±0.22)	0.63 (±0.07)	0.71 (±0.05)	0.63 (±0.07)	0.71 (±0.05)
Field blanks					
FB1	0.95 (±0.12)	0.52 (±0.05)	0.86 (±0.13)	0.54 (±0.08)	0.90 (±0.19)
FB2	1.10 (±0.05)	0.95 (±0.19)	0.93 (±0.06)	0.95 (±0.19)	0.93 (±0.06)
FB3	1.21 (±0.06)	1.20 (±0.08)	1.15 (±0.09)	1.20 (±0.08)	1.15 (±0.09)

[a] *IF* values in these samples were not measured. $IF_{SYR,corr}$ and $IF_{PTA,corr}$ for these samples were estimated from the linear regressions of $1/IF_{P,corr}$ vs. DOC in each dilution series.

[b] The *IF* values were measured for WIN-0.3D, which had an equivalent dilution to the WIN-2 sample.

[c] IF_{FFA} values for PME-NR and PME-R have large uncertainties because there were very small differences between $k'_{PME,DMB}$ and k'_{PME} for a given extract. In this case a small difference in $k'_{PME,DMB}$ can lead to significant change of IF_{FFA}, likely explaining the very different values of IF_{FFA} in PME-R and PME-NR.

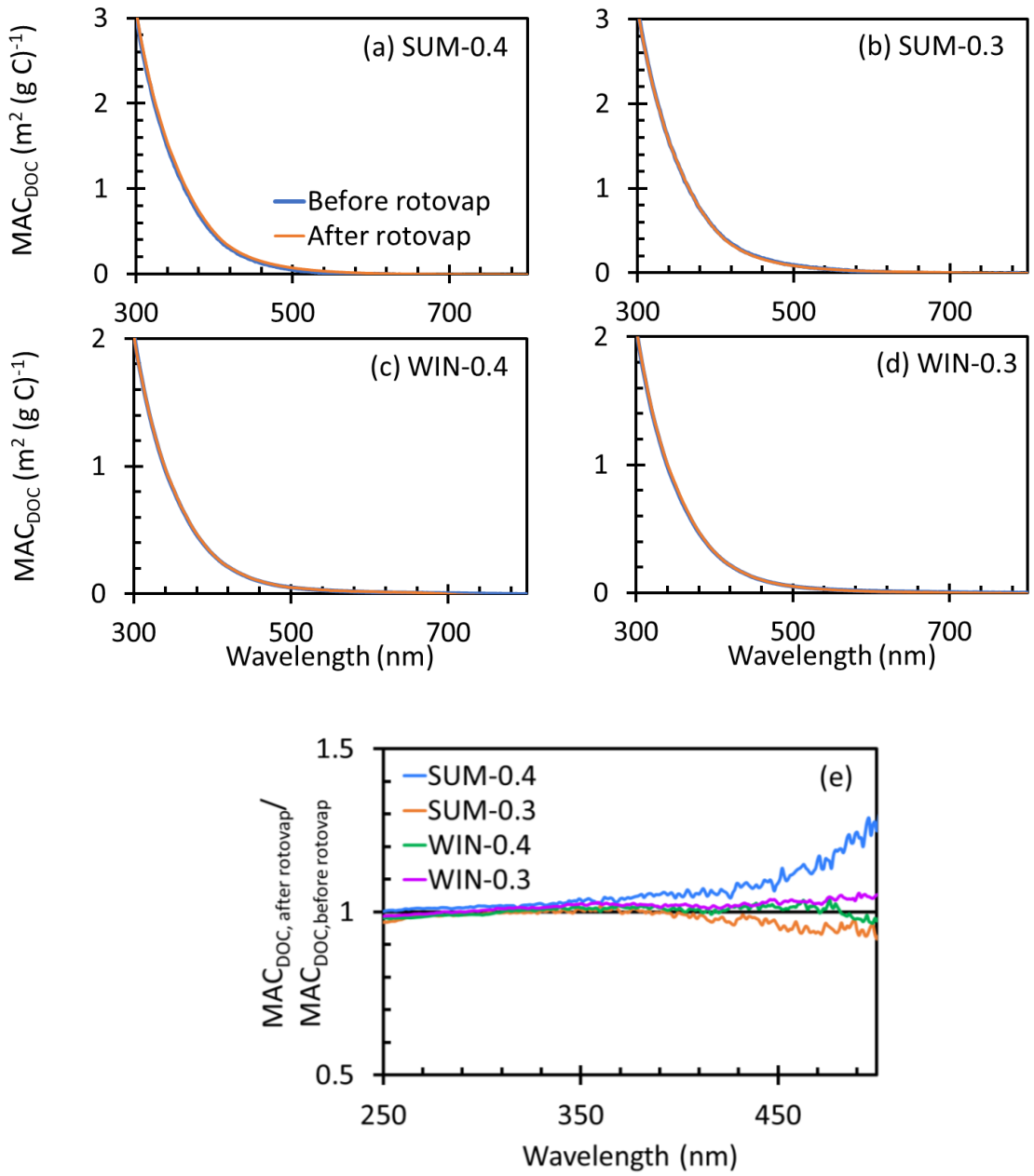

Figure S1. Mass absorption coefficients in particle extracts normalized by dissolved organic carbon before (blue) and after (orange) rotary evaporation for (a) SUM-0.4, (b) SUM-0.3, (c) WIN-0.4, and (d) WIN-0.3. (e) The ratio of MAC_{DOC} after and before rotary evaporation for the four extracts.

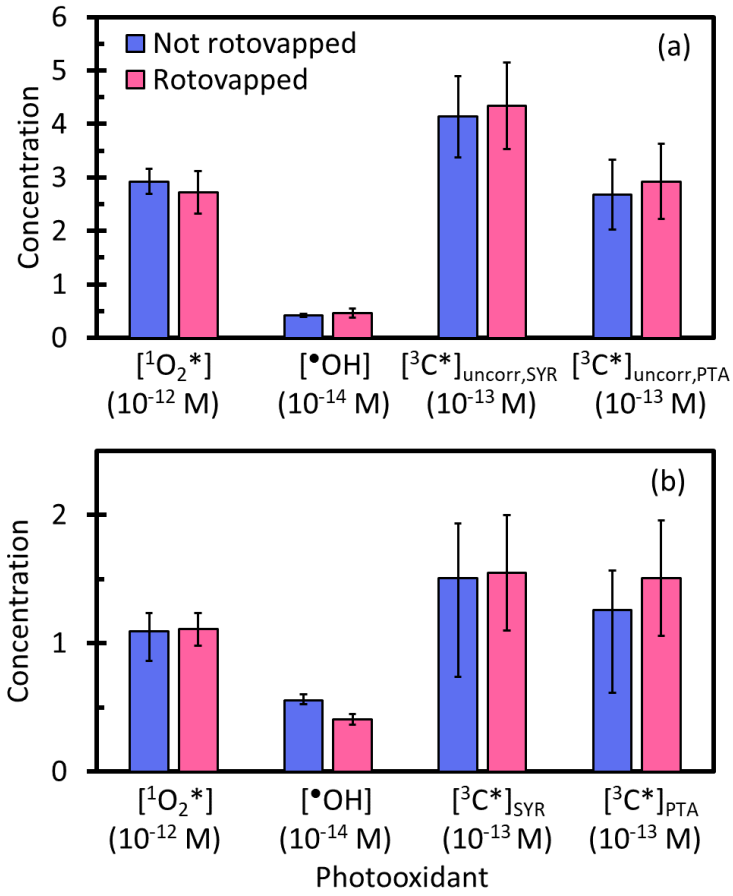

Figure S2. Influence of roto-vapping on steady-state concentrations of $^1O_2$*, •OH, and ^{3}C* in not rotovapped (blue) and rotovapped (red) particle extracts of (a) PME-NR vs. PME-R and (b) WIN-2 vs. WIN-0.3D. In each case, the rotovapped sample was concentrated to the concentration factor (i.e., PM mass/water mass ratio) of the not rotovapped sample. Error bars represents ±1 standard error propagated from uncertainties in the kinetic regression and rate constants. In (a) we show ^{3}C* concentrations that are not *IF*-corrected because IF_{FFA} values for PME-NR and PME-R differ by a factor of nearly two but have large uncertainties (Table S7).

Table S8. Singlet oxygen measurements

Sample ID	$[^1O_2^*]^a$ (10^{-12} M)	$P_{1O2^*}{}^b$ (10^{-7} M s^{-1})	$f_{FFA,1O2^*}{}^c$	$f_{FFA,OH}{}^d$	$10^2 \times \Phi_{1O2^*}{}^e$	$\Phi_{3C^*,SYR}$/ $(\Phi_{1O2^*}/f_\Delta)^f$	$\Phi_{3C^*,PTA}$/ $(\Phi_{1O2^*}/f_\Delta)^g$	$[^3C^*]_{SYR}/[^1O_2^*]^h$	$[^3C^*]_{PTA}/[^1O_2^*]^i$
WIN-10	0.21 (±0.04)	0.45 (±0.08)	0.53 (±0.10)	0.87 (±0.14)	3.1 (±0.5)	0.47 (±0.13)	0.24 (±0.07)	0.23 (±0.07)	0.12 (±0.04)
WIN-2	1.1 (±0.1)	2.4 (±0.3)	0.62 (±0.09)	0.45 (±0.03)	3.1 (±0.4)	0.36 (±0.11)	0.28 (±0.08)	0.14 (±0.04)	0.12 (±0.03)
WIN-0.7	2.3 (±0.4)	5.0 (±0.9)	0.65 (±0.12)	0.61 (±0.02)	2.6 (±0.4)	0.76 (±0.27)	0.29 (±0.09)	0.22 (±0.08)	0.10 (±0.03)
WIN-0.4	4.3 (±0.8)	9.4 (±1.9)	0.69 (±0.14)	0.31 (±0.03)	2.8 (±0.5)	0.84 (±0.30)	0.36 (±0.11)	0.17 (±0.06)	0.09 (±0.03)
WIN-0.3	8.2 (±0.8)	18 (±2)	0.83 (±0.09)	0.14 (±0.01)	3.2 (±0.3)	0.43 (±0.17)	0.27 (±0.09)	0.06 (±0.02)	0.05 (±0.02)
WIN-0.3D	0.98 (±0.13)	2.2 (±0.3)	0.62 (±0.08)	0.64 (±0.07)	2.7 (±0.3)	0.43 (±0.14)	0.38 (±0.12)	0.16 (±0.05)	0.15 (±0.05)
SUM-10	0.33 (±0.19)	0.72 (±0.04)	0.54 (±0.32)	0.20 (±0.02)	1.9 (±1.1)	1.10 (±0.67)	0.24 (±0.15)	0.48 (±0.30)	0.11 (±0.07)
SUM-2	2.2 (±0.2)	4.9 (±0.4)	0.94 (±0.10)	0.12 (±0.01)	2.5 (±0.2)	0.52 (±0.13)	0.17 (±0.05)	0.15 (±0.04)	0.06 (±0.02)
SUM-0.7	5.3 (±0.4)	12 (±1)	1.03 (±0.10)	0.24 (±0.03)	2.3 (±0.2)	0.86 (±0.24)	0.18 (±0.05)	0.13 (±0.04)	0.04 (±0.01)
SUM-0.4	7.7 (±0.6)	17 (±1)	0.91 (±0.09)	0.24 (±0.01)	1.8 (±0.1)	0.96 (±0.27)	0.25 (±0.07)	0.09 (±0.02)	0.04 (±0.01)
SUM-0.3	8.5 (±2.7)	19 (±6)	0.79 (±0.25)	0.20 (±0.02)	1.5 (±0.5)	1.02 (±0.45)	0.28 (±0.12)	0.08 (±0.03)	0.03 (±0.01)
PME-NR	2.9 (±0.2)	6.4 (±0.5)	0.62 (±0.06)	0.25 (±0.02)	2.9 (±0.2)	0.90 (±0.47)	0.48 (±0.27)	0.18 (±0.10)	0.10 (±0.05)
PME-R	2.7 (±0.4)	6.0 (±0.9)	0.59 (±0.09)	0.28 (±0.05)	2.6 (±0.4)	1.22 (±0.32)	0.75 (±0.22)	0.25 (±0.07)	0.15 (±0.04)
Averages									
WIN					2.9 (±0.3)	0.55 (±0.20)	0.22 (±0.05)	0.16 (±0.06)	0.10 (±0.04)
SUM					2.0 (±0.4)	0.89 (±0.23)	0.30 (±0.06)	0.18 (±0.17)	0.06 (±0.03)
Field blanks									
FB1[j]	0.016 (±0.001)		0.81 (±0.15)	8.3 (±4.8)					
FB2	0.021 (±0.001)		0.66 (±0.33)	0.54 (±0.07)					
FB3	0.028 (±0.001)		0.97 (±0.17)	0.73 (±0.09)					

[a] Davis winter solstice sunlight-normalized steady-state concentration of $^1O_2^*$.

[b] Production rate of $^1O_2^*$, calculated as $P_{1O2^*} = [^1O_2^*] \times k'_{H2O}$, where k'_{H2O} is the first-order rate constant for loss of $^1O_2^*$ in H_2O (2.2×10^5 s^{-1}) (Bilski et al., 1997).

[c] Fraction of probe FFA lost due to $^1O_2^*$ in PME diluted with H_2O, calculated as $f_{FFA,1O2^*} = ([^1O_2^*]/2 \times k_{FFA+1O2^*})/k'_{FFA,H2O}$, where $k_{FFA+1O2^*}$ is the second-order rate constant of FFA reacting with $^1O_2^*$ and $k'_{FFA,H2O}$ is the normalized first-order decay rate of FFA in the PME diluted with H_2O.

[d] Fraction of probe FFA lost due to $^\bullet OH$ in PME diluted with H_2O, calculated as $f_{FFA,OH} = ([^\bullet OH] \times k_{FFA+OH})/k'_{FFA,H2O}$, where k_{FFA+OH} is the second-order rate constant of FFA reacting with $^\bullet OH$ (1.5×10^{10} M^{-1} s^{-1}) (Ross and Ross, 1977), assuming the $^\bullet OH$ concentration is the same in the diluted and undiluted portions of PME.

[e] Apparent quantum yield of $^1O_2^*$, calculated as $\Phi_{1O2^*} = P_{1O2^*}/R_{abs}$.

[f] Fraction of oxidizing triplets (determined by SYR) in the total triplet pool (Kaur and Anastasio, 2018). f_Δ is the yield of singlet oxygen from the quenching of triplet states by dissolved oxygen, which we assume is 0.53 (McNeill and Canonica, 2016).

[g] Fraction of oxidizing triplets determined by PTA to the total triplet pool.

[h] Ratio of triplet concentration determined by SYR to the singlet oxygen concentration.

[i] Ratio of triplet concentration determined by PTA to the singlet oxygen concentration.

[j] This field blank sample was contaminated by a pH electrode and other unknown sources.

Table S9. Parameters in hyperbolic fitting between photooxidant concentration and DOC using Eqn. 11

	WIN		SUM	
	a	*b* (M^{-1})	*a*	*b* (M^{-1})
$^1O_2$*	2.8 (± 0.1) ×10^{-10}[a]	6[a]	4.4 (± 0.3) ×10^{-10}	27 (± 4)
$^3C^*_{SYR}$	0.85 (± 0.46) ×10^{-10}	97 (± 86)	1.2 (± 0.4) ×10^{-10}	149 (± 65)
$^3C^*_{PTA}$	0.44 (± 0.05) ×10^{-10}	73 (± 15)	0.31 (± 0.03) ×10^{-10}	84 (± 13)

[a] Since winter samples show no curvature for [$^1O_2$*] with DOC, to fit data with equation 11, *a* was obtained as the slope of linear regression between [$^1O_2$*] and DOC, while *b* was obtained by using a fitted line that passed through only the first 4 data points (Figure S5).

185

Table S10. Second-order rate constants of triplet quenching and reaction with dissolved organic carbon[a]

	$k_{rxn+Q,3C^*}$ (L (mol C)$^{-1}$ s^{-1})		$^3C^*$ probe used
This work	WIN	SUM	
	0.47 × 10^{7}[b]	2.1 (± 0.3) × 10^7	FFA
	7.6 (± 6.8) × 10^7	12 (± 5) × 10^7	SYR
	5.7 (± 1.2) × 10^7	6.6 (± 1.0) × 10^7	PTA
Kaur et al. (2019)[c]	9.3 (±1.3) ×10^7		SYR
Wenk et al. (2013)[d]	(1.3 – 3.9) ×10^7		-

[a] Rate constants are for DOM quenching and reaction with the pool of triplets that are seen by a given probe. FFA, by reacting with $^1O_2$*, is likely seeing the DOM reactivity of the entire triplet pool (i.e., both oxidizing and non-oxidizing triplets), SYR is probing the reactivity of both strongly and weakly
190 oxidizing triplets, while PTA is probing only the strongly oxidizing triplets.

[b] This value was calculated using the *b* value (Table S9) that was estimated by fitting the line of equation 11 between [$^1O_2$*] and DOC through only the first 4 data points (Figure S5).

[c] Value is uncertain because triplet concentrations were not corrected for inhibition of SYR loss caused by DOM.

195 [d] Rate constant measured for quenching of triplets of 2-acetonaphthone and 3-methoxyacetophenone by surface water dissolved organic matter as determined using laser flash photolysis.

Section S2. Kinetic model for singlet oxygen

We first consider a modified equation for the steady-state $^1O_2$* concentration from McNeill et al. (2016) by adding DOC as an additional sink for $^1O_2$*:

$$[^1O_2^*] = \frac{k_{O2+3C*}[^3C^*][O_2]f_\Delta}{k'_{H2O} + k_{rxn+Q,1O2*}[DOC]} \quad (S5)$$

where k_{O2+3C*} is the bimolecular rate constant of O_2 quenching ^{3}C*, [^{3}C*] is the concentration of triplets that can transfer energy to O_2 (i.e., essentially all triplets), [O_2] is the dissolved oxygen concentration, f_Δ is the fraction of oxygen quenching triplets that produces $^1O_2$*, k'_{H2O} is the first-order rate constant for loss of $^1O_2$* by H_2O (2.2×10^5 s^{-1}) (Bilski et al., 1997), and $k_{rxn+Q,1O2*}$ is the bimolecular rate constant of DOC reacting and quenching $^1O_2$*.

While DOC will be an important sink for $^1O_2$* under ALW conditions (Kaur et al., 2019), in our PM extracts it appears the curvature of [$^1O_2$*] with increasing DOC observed in SUM (Fig. 2) is only due to ^{3}C* since triplets are more sensitive to the presence of organics than is $^1O_2$*. Therefore, H_2O is the dominant sink, and the quenching of $^1O_2$* by DOC is negligible (i.e., $k_{rxn+Q,1O2*}[DOC] << k'_{H2O}$). From Kaur et al. (2019), ^{3}C* in PME can be expressed as

$$[^3C^*] = \frac{\left(\frac{j_{abs}\Phi_{ISC}f}{k_{O2+3C*}[O_2]}\right)[DOC]}{1 + \left(\frac{k_{rxn+Q,3C*}}{k_{O2+3C*}[O_2]}\right)[DOC]} \quad (S6)$$

where j_{abs} is the rate constant for light absorption, Φ_{ISC} is the quantum yield of intersystem crossing, f is the fraction of DOC that is in chromophores, and $k_{rxn+Q,3C*}$ is the bimolecular rate constant of DOC reacting with and quenching ^{3}C*.

Substituting this equation for [^{3}C*] into equation S5 (after applying $k_{rxn+Q,1O2*}[DOC] << k'_{H2O}$) yields

$$[^1O_2^*] = \frac{\frac{(\frac{j_{abs}\Phi_{ISC}f}{k_{O2+3C*}[O_2]})[DOC]}{1 + (\frac{k_{rxn+Q,3C}}{k_{O2+3C*}[O_2]})[DOC]} \times k_{O2+3C*}[O_2]f_\Delta}{k'_{H2O}} = \frac{\frac{j_{abs}\Phi_{ISC}f \times f_\Delta}{k'_{H2O}}[DOC]}{1 + (\frac{k_{rxn+Q,3C}}{k_{O2+3C*}[O_2]})[DOC]} \quad (S7)$$

This equation is of the form

$$[^1O_2^*] = \frac{a[DOC]}{1 + b[DOC]} \quad (S8)$$

where

$$a = \frac{j_{abs}\Phi_{ISC}f \times f_{\Delta}}{k'_{H2O}} \quad (S9)$$

$$b = \frac{k_{rxn+Q,3C*}}{k_{O2+3C*}[O_2]} \quad (S10)$$

Since $[^1O_2^*] = P_{1O2^*} / k'_{H2O}$ when DOC is a negligible sink of $^1O_2^*$ (i.e. H_2O is the only sink), the production rate of singlet oxygen can be calculated by

$$P_{1O2^*} = \frac{a[DOC]}{1 + b[DOC]} \times k'_{H2O} \quad (S11)$$

Thus, in our relatively dilute extracts we calculate P_{1O2^*} as $[^1O_2^*] \times k'_{H2O}$ (Eq.10), while for extrapolating to ALW conditions we use Eq. S11 to calculate the $^1O_2^*$ production rate.

Table S11. Parameters used for photooxidant concentration extrapolation

Parameters		WIN	SUM
Average DOC/(PM/H_2O)[a] (mol C L^{-1})/(μg PM/μg H_2O)		16.5	30.7
•OH	$\Delta P_{OH,aq}/\Delta$DOC (M s^{-1}/(mol C L^{-1})[b]	1.6×10^{-6}	-
	$\Delta k'_{OH}/\Delta$DOC (M s^{-1}/(mol C L^{-1})[b]	2.9×10^{8}	2.5×10^{8}
$^1O_2^*$	a[c]	2.8×10^{-10}	4.4×10^{-10}
	b (M^{-1})[c]	6	27
	$k_{DOC+1O2^*}$ (L (mol C)$^{-1}$ s^{-1})[d]	1.0×10^{5}	
$^3C^*_{SYR}$	$\Delta P_{3C^*}/\Delta$DOC (M s^{-1}/(mol C L^{-1})[b]	6.2×10^{-5}	9.2×10^{-5}
	$k_{rxn+Q,3C^*}$ (L (mol C)$^{-1}$ s^{-1})	7.6×10^{7}	12×10^{8}
$^3C^*_{PTA}$	$\Delta P_{3C^*}/\Delta$DOC (M s^{-1}/(mol C L^{-1})[b]	3.4×10^{-5}	2.4×10^{-5}
	$k_{rxn+Q,3C^*}$ (L (mol C)$^{-1}$ s^{-1})	5.7×10^{7}[a]	6.6×10^{7}

[a] Average ratio of DOC to particle mass/water mass ratio for each sample.

[b] Slope of linear regression between production rates or sinks for photooxidant and DOC.

[c] Parameters in regression fit between $[^1O_2^*]$ and DOC using Eqn. 11 in the main text. Production rates of $^1O_2^*$ were calculated using these parameters in Eqn. S11.

[d] Second-order rate constant for loss of $^1O_2^*$ by DOC. The value is estimated using the same approach from Kaur et al. (2019) but is lower than their value of 8.2×10^5 (L (mol C)$^{-1}$ s^{-1}.

Section S3. Modeling the •OH production rate in SUM by photo-Fenton reactions

To simulate bimolecular •OH production as a function of particle mass/water mass ratio in SUM, we assume that photo-Fenton reactions are the dominant sources for •OH. We modeled this using two reactions (SR1 and SR2) and tuned the reactant concentrations so that calculated •OH production rates match measured values.

We simplified the suite of photo-Fenton reactions that produce •OH from hydrogen peroxide (H_2O_2) using two reactions (Benkelberg and Warneck, 1995; Christensen et al., 1993; Mao et al., 2013):

$Fe^{2+} + H_2O_2 \rightarrow Fe^{3+} + {}^{\bullet}OH + OH^-$ $\quad k_1 = 70\ M^{-1}\ s^{-1}$ (SR1)

$FeOH^{2+} + h\nu \rightarrow Fe^{2+} + {}^{\bullet}OH$ $\quad j_{Fe(III)} = 5.6 \times 10^{-3}\ s^{-1}$ (SR2)

We assume that Fe^{2+} and $FeOH^{2+}$ are the dominant Fe(II) and Fe(III) hydroxide species, respectively, which is reasonable at pH 4.2 or lower (Faust and Hoigné, 1990; Morgan and Lahav, 2007). Fe(III)−carboxylate complexes can also undergo photolysis to produce •OH (Southworth and Voelker, 2003; Weller et al., 2014), but we neglect them here. The •OH production rate from SR1 and SR2 is

$$P_{OH} = k_1[Fe^{2+}][H_2O_2] + j_{Fe(III)}[FeOH^{2+}] \quad (S12)$$

Next, we estimate the total dissolved iron and H_2O_2 concentrations so that our calculated P_{OH} approximately matches the measured values in SUM. To do this, we assume that: (1) The ratio of [Fe(II)]/([Fe(II)]+Fe(III)]) is a constant 0.85 during daytime (i.e. during our illumination), (Deguillaume et al., 2005; Weller et al., 2014); (2) H_2O_2 reaches a steady-state concentration during the illumination; (3) The concentrations of dissolved iron and H_2O_2 increase proportionally with concentration factor (PM mass/water mass ratio) in our extracts. By setting dissolved iron and H_2O_2 concentrations to 0.4 μM and 3 μM in SUM-10, respectively, the simulated P_{OH} and [•OH] fit well with the measured values across all dilutions (Figure S4). Meanwhile, the estimated concentrations in SUM-10 are in a reasonable range for dilute cloud/fog water (Anastasio et al., 1994; Deguillaume et al., 2005; Faust et al., 1993). We next extrapolate this simple model to ambient PM conditions with one modification: since the aqueous H_2O_2 concentration cannot increase with the particle mass/water mass ratio without limitation (because $H_2O_{2(aq)}$ can partition into the gas phase), we set an upper limit for $H_2O_{2(aq)}$ of 100 μM, which corresponds to a typical gas-phase H_2O_2 mixing ratio of 1 ppb (Tilgner et al., 2021; Vione et al., 2003) assuming Henry's law equilibrium ($K_H = 10^5$ M atm^{-1}) (Seinfeld and Pandis, 2008). We assume that the H_2O_2(aq) concentration increases proportionally with PM mass/water mass ratio until it reaches 100 μM and then is constant at this value under more concentrated conditions. Our estimated soluble iron concentration of 0.4 μM in SUM-10 predicts a dissolved Fe concentration under ALW conditions (1 μg PM/μg H_2O) of 9.6

mM; we assume this is all dissolved, with no precipitation. This soluble iron concentration is similar to expected dissolved iron concentrations in aqueous aerosols (Gen et al., 2020; Tilgner et al., 2021).

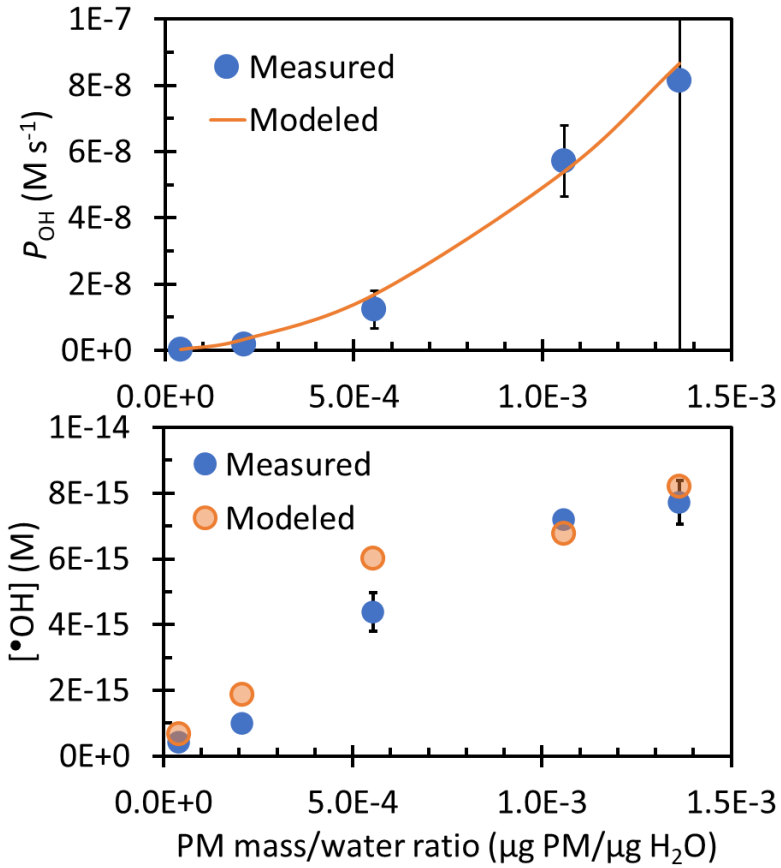

Figure S3. Comparison of measured (blue) and modeled (orange) •OH production rates (top panel) and concentrations (bottom panel) in SUM as a function of particle mass/water mass ratio. The modeled •OH concentration is calculated using the modeled production rate divided by the measured •OH sink (k'_{OH}) at each dilution.

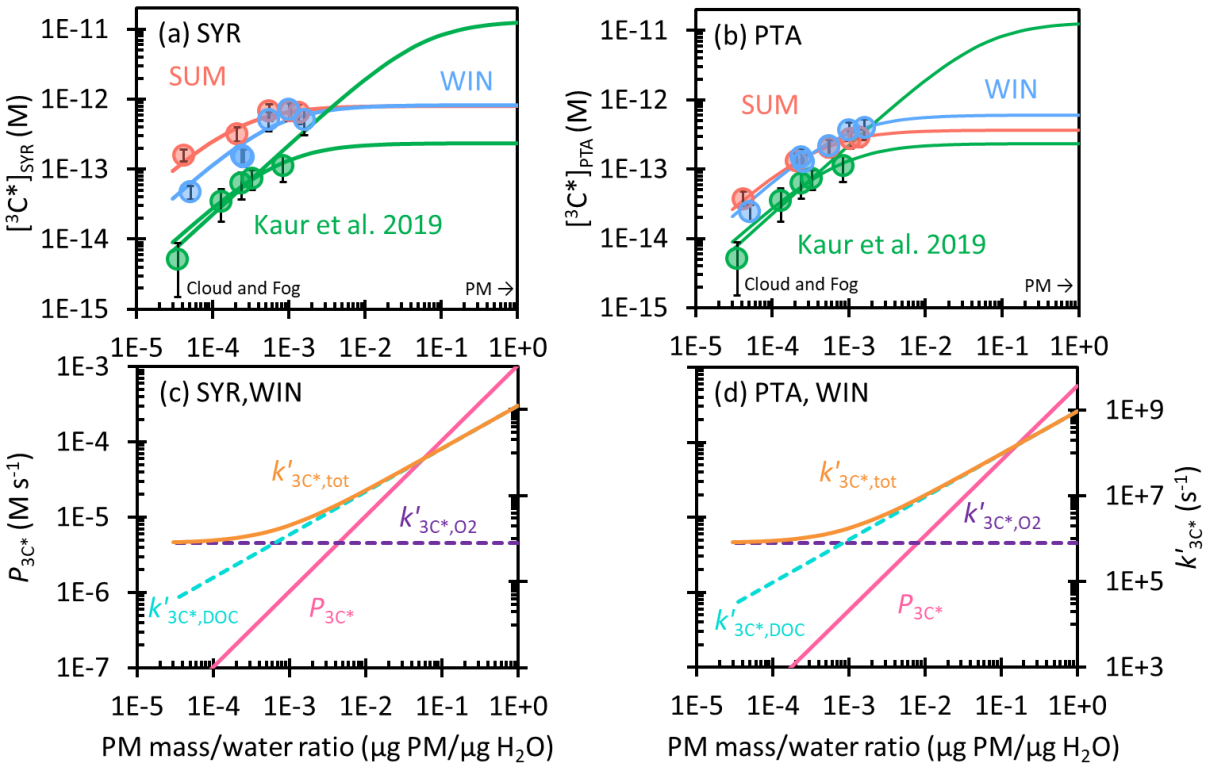

Figure S4. Top row: Triplet excited state concentrations determined by (a) SYR and (b) PTA as a function of particle mass/water mass ratio in WIN extracts (blue) and SUM (red). Solid circles are measured values in dilution experiments, while lines are extrapolations to ALW conditions. Previous measurements and extrapolations (best fit and high estimate) for Davis winter particle extracts are in green (Kaur et al., 2019). Bottom row: Dependence of triplet production rate (red line), and rate constants for ^{3}C* loss, including quenching by oxygen ($k'_{^3C^*,O2}$, purple dashed line), dissolved organic carbon ($k'_{^3C^*,DOC}$, blue dashed line), and total sinks ($k'_{^3C^*,tot} = k'_{^3C^*,O2} + k'_{^3C^*,DOC}$, orange solid line), on particle mass/water mass ratio for the WIN sample. Panels (c) and (d) show data determined using SYR and PTA, respectively.

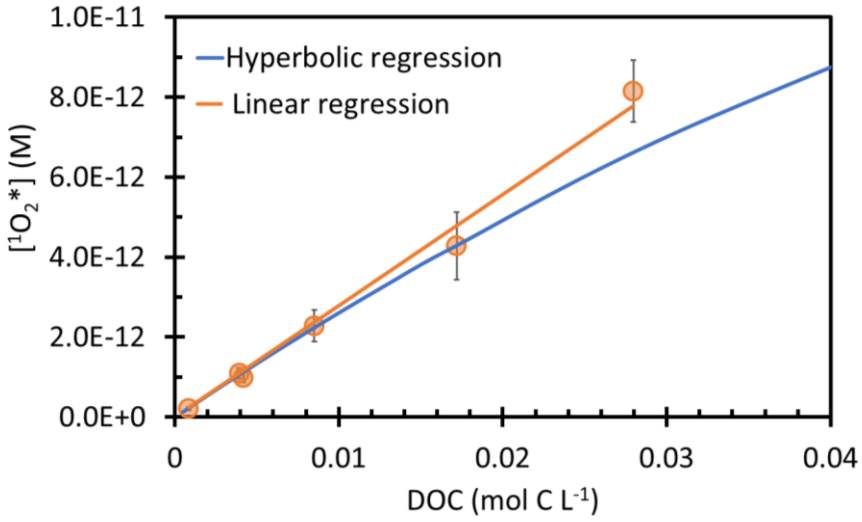

Figure S5. $^1O_2$* concentration as a function of DOC in winter samples (circles). The orange line represents a linear regression fit to all points, while the blue line represents a hyperbolic regression fit to the first 4 data points using equation 11 in the main text.

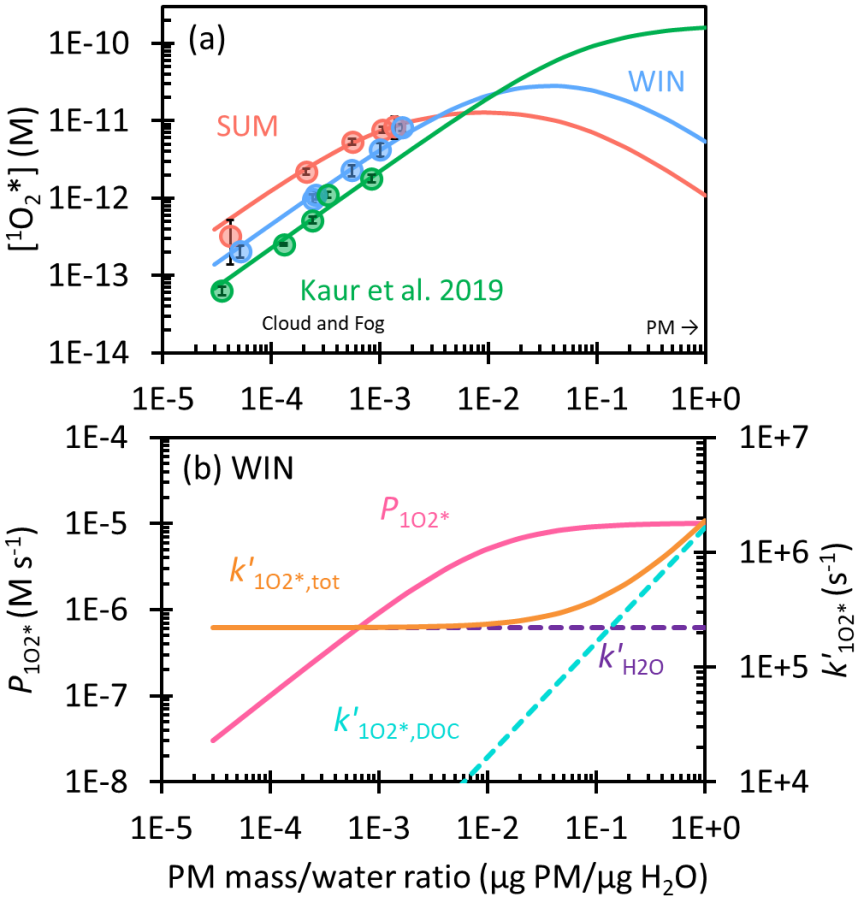

Figure S6. (a) Dependence of singlet molecular oxygen concentration on particle mass/water mass ratio in winter extracts (blue) and summer (red) samples. Solid circles are measured values in dilution experiments, while lines are extrapolations to ALW conditions. Previous measurements and extrapolation with Davis winter particle extracts are in green (Kaur et al., 2019). (b) Singlet oxygen production rate, (P_{1O2*}, red line) and rate constants for $^1O_2$* loss, including deactivation by water (k'_{H2O}, purple), quenching by dissolved organic carbon ($k'_{1O2*,DOC}$, blue), and total sinks ($k'_{1O2*,tot} = k'_{,H2O} + k'_{1O2*,DOC}$, orange), as a function of particle mass/water mass ratio for winter samples.

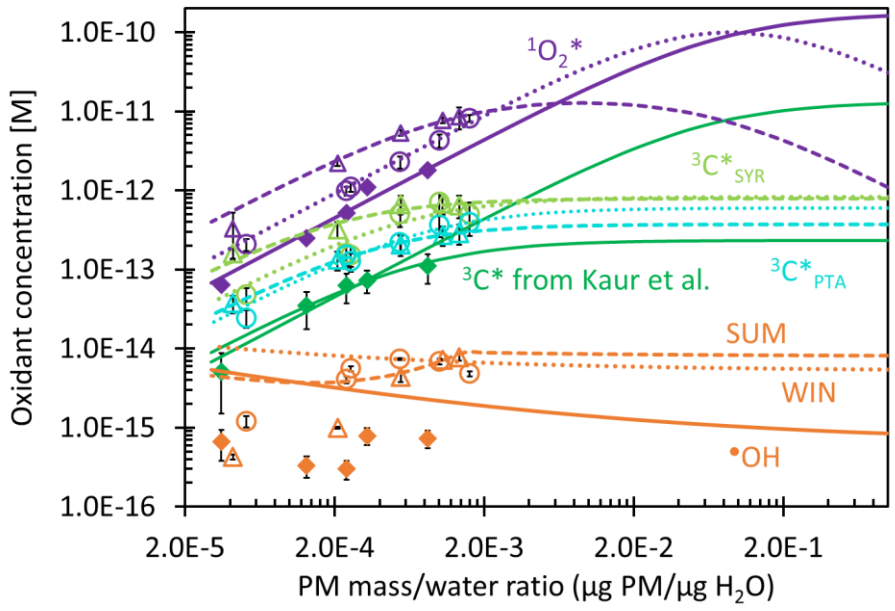

Figure S7. Dependence of photooxidant concentrations on particle mass/water mass ratio in WIN, SUM, and previous Davis winter particle extracts from Kaur et al. (2019). Symbols represent measured values under lab dilution conditions for WIN (open circles), SUM (open triangles), and Kaur et al. (filled diamonds), respectively. Lines represent extrapolations of experimental data to aerosol liquid water conditions for WIN (dotted lines), SUM (dashed lines), and Kaur et al. (solid lines) samples. Singlet oxygen concentrations are in purple; triplet concentrations are in light green for SYR-determined values, blue for PTA-determined values, and dark green for data from Kaur et al.; hydroxyl radical concentrations are in orange. The lines for •OH are generally higher than the experimental measurements because the extrapolations include mass transfer of gas-phase hydroxyl radical to the drop/particle. The gas phase does not appear to be a significant source or sink of particle-phase $^3C^*$ or $^1O_2^*$.

References

Anastasio, C., Faust, B. C. and Allen, J. M.: Aqueous phase photochemical formation of hydrogen peroxide in authentic cloud waters, J. Geophys. Res., 99(D4), 8231, doi:10.1029/94JD00085, 1994.

Anastasio, C. and McGregor, K. G.: Chemistry of fog waters in California's Central Valley: 1. In situ photoformation of hydroxyl radical and singlet molecular oxygen, Atmos. Environ., 35(6), 1079–1089, doi:10.1016/S1352-2310(00)00281-8, 2001.

Benkelberg, H.-J. and Warneck, P.: Photodecomposition of Iron(III) Hydroxo and Sulfato Complexes in Aqueous Solution: Wavelength Dependence of OH and SO4- Quantum Yields, J. Phys. Chem., 99(14), 5214–5221, doi:10.1021/j100014a049, 1995.

Bilski, P., Holt, R. N. and Chignell, C. F.: Properties of singlet molecular oxygen in binary solvent mixtures of different polarity and proticity, J. Photochem. Photobiol. A, 109(3), 243–249, doi:10.1016/S1010-6030(97)00147-0, 1997.

Canonica, S. and Laubscher, H.-U.: Inhibitory effect of dissolved organic matter on triplet-induced oxidation of aquatic contaminants, Photochem. Photobiol. Sci., 7(5), 547, doi:10.1039/b719982a, 2008.

Christensen, H., Sehested, K. and Løgager, T.: The reaction of hydrogen peroxide with Fe(II) ions at elevated temperatures, Radiation Physics and Chemistry, 41(3), 575–578, doi:10.1016/0969-806X(93)90022-M, 1993.

Deguillaume, L., Leriche, M., Desboeufs, K., Mailhot, G., George, C. and Chaumerliac, N.: Transition metals in atmospheric liquid phases: sources, reactivity, and sensitive parameters., Chem. Rev., 105(9), 3388–3431, doi:10.1021/cr040649c, 2005.

Faust, B. C., Anastasio, C., Allen, J. M. and Arakaki, T.: Aqueous-phase photochemical formation of peroxides in authentic cloud and fog waters., Science, 260(5104), 73–75, doi:10.1126/science.8465202, 1993.

Faust, B. C. and Hoigné, J.: Photolysis of Fe (III)-hydroxy complexes as sources of OH radicals in clouds, fog and rain, Atmospheric Environment. Part A. General Topics, 24(1), 79–89, doi:10.1016/0960-1686(90)90443-Q, 1990.

Gen, M., Zhang, R., Li, Y. and Chan, C. K.: Multiphase photochemistry of iron-chloride containing particles as a source of aqueous chlorine radicals and its effect on sulfate production, Environ. Sci. Technol., 54(16), 9862–9871, doi:10.1021/acs.est.0c01540, 2020.

Kaur, R. and Anastasio, C.: First measurements of organic triplet excited states in atmospheric waters., Environ. Sci. Technol., 52(9), 5218–5226, doi:10.1021/acs.est.7b06699, 2018.

Kaur, R., Labins, J. R., Helbock, S. S., Jiang, W., Bein, K. J., Zhang, Q. and Anastasio, C.: Photooxidants from brown carbon and other chromophores in illuminated particle extracts, Atmos. Chem. Phys., 19(9), 6579–6594, doi:10.5194/acp-19-6579-2019, 2019.

Ma, L., Worland, R., Tran, T. and Anastasio, C.: An evaluation of probes to measure oxidizing triplet excited states in aerosol liquid water, Environ. Sci. Technol., In press, 2023.

Mao, J., Fan, S., Jacob, D. J. and Travis, K. R.: Radical loss in the atmosphere from Cu-Fe redox coupling in aerosols, Atmos. Chem. Phys., 13(2), 509–519, doi:10.5194/acp-13-509-2013, 2013.

McNeill, K. and Canonica, S.: Triplet state dissolved organic matter in aquatic photochemistry: reaction mechanisms, substrate scope, and photophysical properties., Environ. Sci. Process. Impacts, 18(11), 1381–1399, doi:10.1039/c6em00408c, 2016.

Morgan, B. and Lahav, O.: The effect of pH on the kinetics of spontaneous Fe(II) oxidation by O2 in aqueous solution--basic principles and a simple heuristic description., Chemosphere, 68(11), 2080–2084, doi:10.1016/j.chemosphere.2007.02.015, 2007.

Ross, F. and Ross, A. B.: Selected specific rates of reactions of transients from water in aqueous solution. III. Hydroxyl radical and perhydroxyl radical and their radical ions, Historical Energy Database (United States)., 1977.

Seinfeld, J. and Pandis, S.: Atmospheric chemistry and physics: from air pollution to climate change. John Wiley & Sons, 2016.

Smith, J. D., Kinney, H. and Anastasio, C.: Aqueous benzene-diols react with an organic triplet excited state and hydroxyl radical to form secondary organic aerosol., Phys. Chem. Chem. Phys., 17(15), 10227–10237, doi:10.1039/c4cp06095d, 2015.

Smith, J. D., Kinney, H. and Anastasio, C.: Phenolic carbonyls undergo rapid aqueous photodegradation to form low-volatility, light-absorbing products, Atmos. Environ., 126, 36–44, doi:10.1016/j.atmosenv.2015.11.035, 2016.

Southworth, B. A. and Voelker, B. M.: Hydroxyl radical production via the photo-Fenton reaction in the presence of fulvic acid., Environ. Sci. Technol., 37(6), 1130–1136, doi:10.1021/es020757l, 2003.

Tilgner, A., Schaefer, T., Alexander, B., Barth, M., Collett Jr., J. L., Fahey, K. M., Nenes, A., Pye, H. O. T., Herrmann, H. and McNeill, V. F.: Acidity and the multiphase chemistry of atmospheric aqueous particles and clouds, Atmos. Chem. Phys., 21(17), 13483–13536, doi:10.5194/acp-21-13483-2021, 2021.

Tratnyek, P. G. and Hoigne, J.: Oxidation of substituted phenols in the environment: a QSAR analysis of rate constants for reaction with singlet oxygen, Environ. Sci. Technol., 25(9), 1596–1604, 1991.

Vione, D., Maurino, V., Minero, C. and Pelizzetti, E.: The atmospheric chemistry of hydrogen peroxide: a review., Ann. Chim., 93(4), 477–488, 2003.

Weller, C., Tilgner, A., Bräuer, P. and Herrmann, H.: Modeling the impact of iron-carboxylate photochemistry on radical budget and carboxylate degradation in cloud droplets and particles., Environ. Sci. Technol., 48(10), 5652–5659, doi:10.1021/es4056643, 2014.

Wenk, J., Eustis, S. N., McNeill, K. and Canonica, S.: Quenching of excited triplet states by dissolved natural organic matter., Environ. Sci. Technol., 47(22), 12802–12810, doi:10.1021/es402668h, 2013.

Wenk, J., von Gunten, U. and Canonica, S.: Effect of dissolved organic matter on the transformation of contaminants induced by excited triplet states and the hydroxyl radical., Environ. Sci. Technol., 45(4), 1334–1340, doi:10.1021/es102212t, 2011.